Journal of Materials Processing Tech. 331 (2024) 118501

Contents lists available at ScienceDirect

Journal of Materials Processing Tech.

journal homepage: www.elsevier.com/locate/jmatprotec

Research article

Contact-force-based closed-loop control of shell structure additive manufacturing with continuous-fiber-reinforced polymer composites

Yuexin Yang [a], Yi Zhou [a], Molong Duan [a,b,*]

[a] *Department of Mechanical and Aerospace Engineering, The Hong Kong University of Science and Technology, Hong Kong, China*
[b] *HKUST Shenzhen-Hong Kong Collaborative Innovation Research Institute, Futian, Shenzhen, China*

ARTICLE INFO

Keywords:
Continuous fiber-reinforced composites
Additive manufacturing
Closed-loop control
Contact force
Trajectory generation

ABSTRACT

Additive manufacturing (AM) is an automated process for fabricating complex structures, especially for continuous fiber-reinforced polymer (CFRP) composites with exceptional mechanical performance and reduced weight. The extrusion-based CFRP-AM process has been widely adopted but faces challenges with insufficient impregnation/adhesion and lack of geometrical accuracy. Existing research efforts exploit various mechatronics approaches and printing parameter adjustment techniques to enhance CFRP quality. Nevertheless, most of them are static or slow-varying; thus, they cannot dynamically adjust to local geometrical features and faults, which are particularly representative of the CFRP-AM process in high-curvature regions. To enable dynamic and rapid adjustment, this study exploits contact forces as major real-time feedback signals to dynamically control the feed velocity, layer height, and fiber extrusion rate. To create a continuous feedback control environment for dynamic adjustment, the study also proposes a novel helical CFRP-AM printing trajectory generation method for closed shell structures, such that the helical angles indirectly adjust the layer height of the parts. A material extrusion CFRP-AM platform combining a co-extrusion nozzle, an industrial robot, a six-degree-of-freedom load cell, and a real-time closed-loop control system is built to verify the proposed control framework. Three representative case studies are introduced to show the enhancements of the closed-loop CFRP-AM process, particularly in layer height adjustment, high-speed printing, and large curvature regions.

1. Introduction

Continuous-fiber-reinforced polymer (CFRP) composites are extensively utilized in various applications such as aerostructures and automobiles due to their exceptional properties of lightweight, high stiffness, and excellent strength [1]. Compared to conventional fiber-reinforced material manufacturing techniques (e.g., winding, pultrusion, vacuum forming, co-weaving, powder impregnation, and compression process), additive manufacturing (AM) has the advantage of in the fabrication of parts with complex geometry without mold at a high automation level [2]. The AM with carbon fiber-reinforced materials is classified into short-fiber and continuous-fiber composites. Continuous CFRP-AM offers substantial advantages over short fiber composites, exhibiting significantly enhanced strength, stiffness, and volume ratio [3], particularly with fiber path optimization algorithms satisfying multiple design objectives [4].

CFRP-AM is typically achieved by material extrusion, directed energy deposition, and laminated object manufacturing processes [5], among which the material extrusion method is the most widely adopted due to its straightforward working principle, abundant material selections, and low cost [6]. Material extrusion CFRP-AM feeds fiber prepreg (or dry fiber) into a heated nozzle, infiltrates the fiber with molten thermoplastic or thermoset resins, and then extrudes from the nozzle to build a composite structure [7]. The working principle is similar to the conventional plastic material extrusion 3D printer with extra fiber feeding and cutting mechanisms. Despite the convenience of the material extrusion type of CFRP-AM process, it still suffers from quality issues. Wang et al. [8] found that insufficient impregnation will weaken the bonding between materials and lead to the tensile strength decrease of printed parts. Another bonding issue, generally called lack of adhesion, also negatively affects the printing quality [9]. Besides, geometrical inaccuracy often appears [10], particularly in the fabrication of high-curvature regions with stiffened prepreg fibers. These quality issues have been shown to significantly impact the mechanical performances of fabricated parts and require more dedicated control [11].

The introduction of additional mechatronics hardware and energy

* Corresponding author at: Department of Mechanical and Aerospace Engineering, The Hong Kong University of Science and Technology, Hong Kong, China.
E-mail address: duan@ust.hk (M. Duan).

https://doi.org/10.1016/j.jmatprotec.2024.118501
Received 16 May 2024; Received in revised form 24 June 2024; Accepted 7 July 2024
Available online 27 July 2024

sources are exploited to enhance the printing quality. Li et al. [12] utilized microwaves for instantaneous and volumetric heating in the CFRP-AM process to achieve strength-enhanced printing results. Yao et al. [13] developed a layer-wise, in-process laser treatment method for improving interlayer bonding. Liu et al. [14] achieved good impregnation and high fiber fraction with high pressure provided by a novel micro-screw in-situ extrusion system. Still, these methods are limited in addressing the printing quality issues that are closely related to the local geometrical features, printing trajectory, and time-varying printing conditions [10]. These local features are very representative in the CFRP-AM process, and thus require dynamic real-time adjustment and closed-loop control.

Closed-loop control has been widely investigated in other extrusion-based AM applications to enhance printing performance. Chen et al. [15] developed an image-based in-situ monitoring system to generate compensation signals, thus solving over-extrusion at corner regions while maintaining geometrical accuracy. Besides, Mercado et al. [16] developed an effective nozzle monitoring system that helps prevent nozzle clogging errors. Currently, investigations of the closed-loop control of the CFRP-AM process are relatively limited. Lu et al. [17] developed a deep-learning-assisted real-time defect detection and closed-loop control algorithm to enhance the printing quality and geometrical accuracy of the fibers, addressing CFRP quality issues at high curvature regions. The vision system detects possible misalignments and adjusts the printing parameters in a dynamic setting. However, the vision-based closed-loop feedback is relatively slow due to the limited onboard computational resources. It is also affected by the limited camera view angle, environment lighting variation, and layer-to-layer misidentification. Recent investigations have indicated that the contact force between the nozzle and the printed part may shed light on the possibilities of closed-loop control. Although the CFRP-AM processes are typically implemented with an extrusion system, the contact force is significantly different from material extrusion processes since there is a solid connection (i.e., the fiber) between the nozzle and the printing platform [18]. Lee et al. [19] investigated the bonding between layers in CFRP and concluded that the normal pressure force contributes to intralayer adhesion. Following the same trend, Zhang et al. [20] tried to increase the pressure by decreasing the hatch spacing or adding a pressure roll. Both groups observed a certain level of bonding enhancement, leading to increased pressure. At the same time, they also observed that excessive pressure force may increase the stress of the fibers, cause fiber abrasion, and eventually affect the fiber continuity and the mechanical properties of the composite [21]. Zhang et al. [22] further classified the CFRP-AM process force into traction force, nominal force, ironing force, and viscous force to highlight the delicacy of the forces and their relationship to the printing quality. It has also been pointed out that the force acts as a desirable monitoring signal for potential CFRP defects [18].

Despite the contact force in the CFRP-AM process providing desirable monitoring signals, there is currently a lack of investigation into real-time closed-loop feedback control with the contact force signal. In contrast to the existing invariable printing parameters during the open-loop CFRP-AM process, the closed-loop system with feedback control and adjustable printing parameters enables online fault detection and produces strategies in time to avoid printing defects, which facilitates manufacturing high-quality and complex-shaped CFRP parts with high automation. The challenge to achieve this is attributed to the high dynamics and complexity of the printing process and the strong need for printing continuity. To fill this gap, a closed-loop controlled CFRP-AM process that dynamically exploits the contact force to adjust the process and trajectory is established in this work. To create a continuous environment for control, a helical trajectory generation method without fiber cutting is established for closed shell structures. In addition, an effective closed-loop contact force feedback controller, including the adaptation of helical angle and layer height, velocity control with side force feedback, and fiber tension control with tangential force feedback, is designed. Finally, a robotic experimental platform and three verification case studies are presented to show the effectiveness of the proposed controller in enhancing printing quality. The main novelties of this paper can be summarized as follows:

- A systematic mathematical helical printing trajectory generation enabling dynamical adjustment of layer height is proposed for closed shell structures. The helical printing path avoids fiber cutting and keeps the printing continuity, enabling continuous closed-loop control while preserving the desired shape.
- The contact force in the CFRP-AM process is firstly exploited for closed-loop feedback control. The system enables dynamically adjusting the printing speed, fiber extrusion, and layer height. The real-time feedback controller applied on the closed shell structures with helical printing path has been proven to enhance fiber tracking accuracy and surface quality in fabricating high-quality complex-shape CFRP parts.

2. Helical trajectory generation for closed shell structures

The CFRP-AM process differs from the conventional material extrusion process due to the rigid fiber connection between the nozzle and the printing platform. As a result, fiber cutting is typically required when the printing trajectory switches at different regions, layers, or paths. Fiber cutting causes different adherence characteristics and contact dynamics, so reducing the number of fiber cuttings required to manufacture a single part is desirable. Reducing the fiber cutting also aligns with this work's focus on the dynamic force control of the CFRP-AM processes. Therefore, inspired by Bettini et al. [23], this work proposes a mathematical helical trajectory generation method for closed shell structures instead of the conventional layer-by-layer build-up that requires fiber cutting at different layers. This helical trajectory provides a continuous feedback (FB) control testing environment for the CFRP-AM process.

2.1. Closed shell structure and reference helical printing path

Consider a continuous shell structure characterized by the continuous change of its cross-sections around a given center line. Assume the total height is H, the center line is defined as $\mathbf{x}_c(h) : [0, H]\rightarrow\mathbb{R}^2$ where h is height along the build-up direction. It is also assumed that $\mathbf{x}_c(h)$ is first order continuous for further dynamic adjustment of the printing process. With the centerline defined, the entire close structure is defined with the layer-dependent cross-section function $\mathbf{c}_{s0}(l, h) : [0, 1] \times [0, H]\rightarrow\mathbb{R}^2$ where l is the percentage of the total length at each cross-section. The cross-section at height h is defined in reference frames origined at $\mathbf{x}_c(h)$. Accordingly, the shell structure cross-section shape in the ground frame is given by

$$\mathbf{c}_s(l, h) = \mathbf{c}_{s0}(l, h) + \mathbf{x}_c(h) \tag{1}$$

Along each cross-section, l increases from 0 to 1 in a counterclockwise manner. This definition can be interpreted as an extension of the polar coordinate definition. Similar to the center line, the $\mathbf{c}_s(l, h)$ is assumed to be first-order continuous, such that their Jacobians are continuous and are defined as

$$\mathbf{J}_{cl}(l, h) = \frac{\partial \mathbf{c}_s(l, h)}{\partial l},\ \mathbf{J}_{cz}(l, h) = \frac{\partial \mathbf{c}_s(l, h)}{\partial h} \tag{2}$$

The shell structure is assumed to be closed and continuous at each cross-section, satisfying

$$\mathbf{c}_s(0, h) = \mathbf{c}_s(1, h) \tag{3}$$

$$\mathbf{J}_{cl}(0, h) = \mathbf{J}_{cl}(1, h),\ \mathbf{J}_{cz}(0, h) = \mathbf{J}_{cz}(1, h) \tag{4}$$

The curve $\mathbf{c}_s(0, h)$ formulates the spatial developing line, as shown in

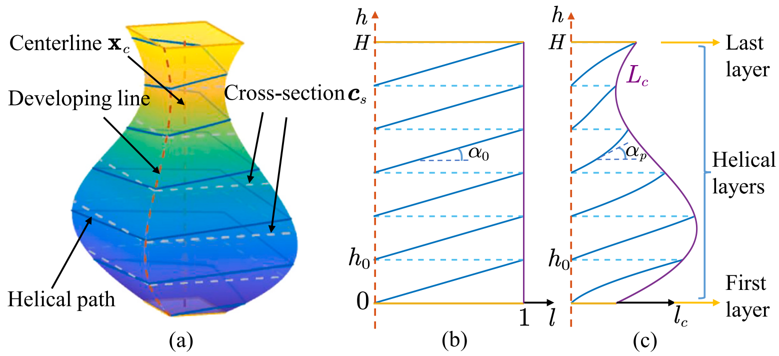

Fig. 1. Schematics of helical printing path of a shell structure without fiber cutting. (a) Helical path on the 3D structure, (b)-(c) 2D mapping with percentage of the total length and total length as the horizontal axis, respectively.

Fig. 1. To enable efficient calculation, a curve length function at each cross-section height is given by

$$l_c(l,h) = \int_0^l |\mathbf{J}_{cl}(\xi,h)|d\xi \tag{5}$$

Note that

$$l_c(0,h) = 0,\ l_c(1,h) = L_c(h) \tag{6}$$

where $L_c(h)$ is the total length of the cross-section at height h. Note that $L_c(h)$ is also first-order continuous due to the first-order continuous condition of $\mathbf{c}_s(l,h)$. The 2D map shown in Fig. 1(b) and (c) demonstrates the relationship between l and l_c at different height h.

A helical printing path is defined along the shell structure to perform the printing. Define the reference layer height as h_0 similar to the pitch of a screw defining the axial distance of the helix in one complete revolution. The helical printing path is illustrated in Fig. 1(a). The helical region spans most of the build-up apart from the first and the last layer; its height H_h is H. The approximate helical angle is defined with the layer height, i.e., $\alpha_0 = h_0$. It should be noted that this is not the physical printing angle of the printing path upwards; the physical printing angle is calculated by

$$\alpha_p(h) = \frac{\alpha_0}{L_c(h)} \tag{7}$$

Note that this local physical angle continuously changes with respect to height and regional length. In the following feedback design, the term α_0 is dynamically controlled to achieve adjustable printing layer height. The total number of turns $N_s \in \mathbb{R}$ can be obtained by

$$N_s = H_s/h_0 \tag{8}$$

Define the entire printing references as $\mathbf{r} = \{r_x, r_y, r_z\}^\top$; these printing references can be conveniently parameterized with the non-dimensional turns of the printing path l_t, the z-axis printing path is defined as

$$r_z(l_t) = \begin{cases} 0 & l_t \in (0,1) \\ (l_t-1)h_0 & l_t \in (1, N_s+1) \\ H & l_t \in [N_s+1, N_s+2] \end{cases} \tag{9}$$

The x- and y-axes printing paths are defined as

$$\{r_x(l_t), r_y(l_t)\}^\top = \mathbf{c}_s(l_m(l_t), r_z(l_t)) \tag{10}$$

where $r_z(l_t)$ is defined in Eq. (9) while $l_m \in [0,1]$ refers to the remainder of the turns, i.e.,

$$l_m = l_t - \lfloor l_t \rfloor \tag{11}$$

where the operation $\lfloor l_t \rfloor$ refers to the largest integer no larger than l_t.

This definition of the printing path established a new slicing strategy for closed shell structures from CAD models. Unlike the conventional layer-by-layer approach to generate printing path, the unorder points on the sliced closed contours are reorganized, starting from the positive x-axis direction and proceeding in an anticlockwise manner. Subsequently, an interpolation technique is applied to transform the contour into the aforementioned cross-section model. The locations at $l = 0$ and $l = l_0 \in [0,1]$ on each contour are depicted in Fig. 2(b). With the closed shell structure defined, the generation of a helical printing path is illustrated in Fig. 2(c).

2.2. Reference velocity planning along the helical printing path

With the defined closed shell structure shape, a planned and dynamically adjustable velocity profile converts the printing path to the motion trajectory of the robotic manipulators. The detailed collaboration between the shell structure geometry, printing path, and velocity control is shown in the flowchart in Fig. 3. The velocity planning along the helical printing path requires the curve length $s(l_t)$ calculation. As a general framework, the curve length is given by

$$s(l_t) = \int_0^{l_t} |d\mathbf{r}| = \int_0^{l_t} \left|\frac{\partial \mathbf{r}(l)}{\partial l}\right| dl \tag{12}$$

This curve length depends on the layer of the trajectory and thus needs to be calculated separately. For the first layer (i.e., $l_t \in [0,1)$), the curve length is given by

$$s(l_t) = l_c(l_t, 0),\ \text{when } l_t \in [0,1) \tag{13}$$

For the helical regions (i.e., $l_t \in [1, N_s+1)$), the calculation of the curve length requires the gradients of the printing path, given by

$$\frac{\partial \mathbf{r}}{\partial l_t} = \begin{Bmatrix} \mathbf{J}_{cl}(l_m, r_z) + h_0 \mathbf{J}_{cz}(l_m, r_z) \\ h_0 \end{Bmatrix} \tag{14}$$

Accordingly, the curve length is given by

$$\begin{aligned} s(l_t) &= L_c(0) + h_0 \int_0^{l_t} \lambda(l_m, r_z) dl,\ \text{when } l_t \in [1, N_s+1), \\ \lambda(l_m, r_z) &= \sqrt{\left(\frac{J_{cl,x}}{h_0} + J_{cz,x}\right)^2 + \left(\frac{J_{cl,y}}{h_0} + J_{cz,y}\right)^2 + 1} \end{aligned} \tag{15}$$

In the last layer, the curve length is given by

$$\begin{aligned} s(l_t) &= s(N_s+1) + \int_0^{l_t} |\mathbf{J}_{cl}(l_t - N_s - 1, H)| dl, \\ &\text{when } l_t \in [N_s+1, N_s+2] \end{aligned} \tag{16}$$

accounting for the possibility that the starting of the last layer may not start from the developing line. Note that the curve length $s(l_t)$ monotonically increase based on the definitions. Therefore, l_t and s formulate

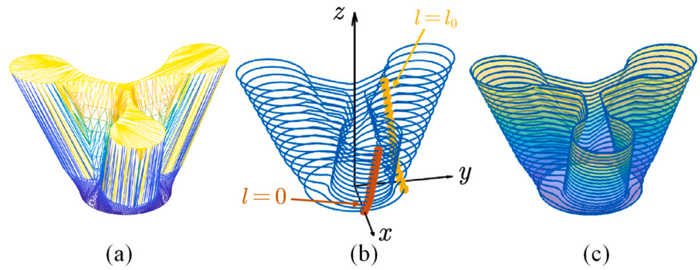

Fig. 2. Path generation procedure of a tri-tube connector. (a) CAD model, (b) sliced model, and (c) helical printing path.

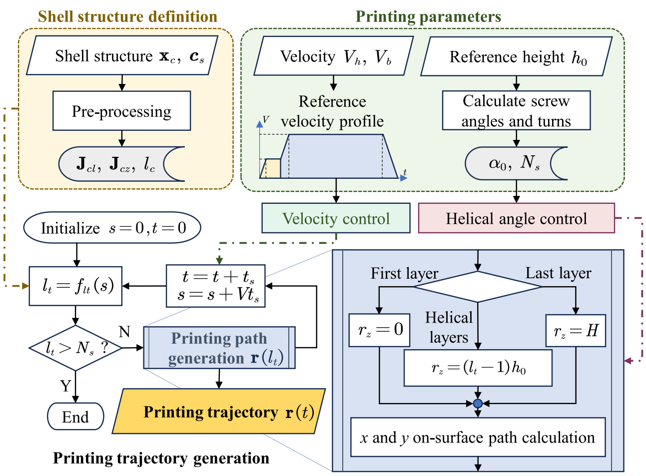

Fig. 3. Flowchart of helical trajectory generation and control for closed shell structures.

a one-to-one projection. Define the inverse relationship to be

$$l_t = f_{lt}(s). \tag{17}$$

The assumed reference printing velocity is plotted in Fig. 4. With a velocity profile, the printing path can be converted to a trajectory for the motion platforms to follow. For the helical printing paths, two representative velocities V_b and V_h are adopted. The first layer is assumed to have a lower velocity V_b to enhance the adhesion to the platform. The rest of the layers are printed with velocity V_h. A constant acceleration A_f is adopted. It is assumed that the printing path is relatively long such that the V_b and V_h can always be achieved. The critical time spans required to reach the critical positions in the reference velocity profiles in Fig. 4 are given by

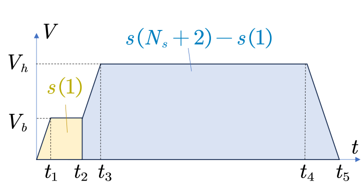

Fig. 4. Reference velocity planning of the helical printing trajectory.

$$\begin{cases} t_1 = \dfrac{V_b}{A_f} \\ t_2 = t_1 + \dfrac{s(1) - s_1}{V_b} \\ t_3 = t_2 + \dfrac{V_h - V_b}{A_f} \\ t_4 = t_3 + \left(s(N_s+2) - s(1) - \dfrac{V_h^2 - V_b^2}{2A_f} - \dfrac{V_h^2}{2A_f} \right) \Big/ V_h \\ t_5 = t_4 + \dfrac{V_h}{A_f} \end{cases} \tag{18}$$

Accordingly, the characteristic length of the curve is given by

$$\begin{cases} s_1 = \dfrac{V_b^2}{2A_f} \\ s_2 = s(1) \\ s_3 = s_2 + \dfrac{V_h^2 - V_b^2}{2A_f} \\ s_4 = s_3 + \left(s(N_s+2) - s(1) - \dfrac{V_h^2 - V_b^2}{2A_f} - \dfrac{V_h^2}{2A_f} \right) \\ s_5 = s(N_s+2) \end{cases} \tag{19}$$

The reference curve length with respect to time follows the given relationship

$$s(t) = \begin{cases} \dfrac{A_f t^2}{2}, & t \in (0, t_1) \\ s_1 + V_b(t - t_1), & t \in (t_1, t_2) \\ s_2 + V_b(t - t_2) + \dfrac{A_f (t - t_2)^2}{2}, & t \in (t_2, t_3) \\ s_3 + V_h(t - t_3), & t \in (t_3, t_4) \\ s_4 + V_h(t - t_4) - \dfrac{A_f (t - t_4)^2}{2}, & t \in (t_4, t_5) \end{cases} \tag{20}$$

This relationship converts back to the fiber path command in each time step t_s through the inverse function defined in Eq. (17). The time-domain printing trajectory $\mathbf{r}(t)$ with velocity planning is thus derived and is used as the reference signal for the AM printers. The flowchart of the helical trajectory generation process is illustrated in Fig. 3. Note that although the reference trajectory generation in Eq. (18)~(20) builds on a representative velocity profile, the current framework allows variations in the velocity with a dynamically evaluated curve length and trajectory generation. This capability with velocity variation is key to the following closed-loop control detailed in Section 3.

The fiber and thermoplastic matrix material extrusion lengths are assumed to be proportional to the curve length, respectively. They are given by

$$L_f = \beta_f s, \; L_m = \beta_m s \tag{21}$$

where β_f and β_m represent the extrusion rate ratio of fiber and matrix, respectively. Since the fiber length is very close to the actual curve length, β_f is expected to be very close to one. Therefore, although the term β_f dynamically changes with the feedback signal, its deviation from one is bound to be a small value.

3. Contact force based closed-loop control of CFRP-AM process

The fiber contact force is a very representative monitoring signal for the printing quality. At all time instants, the contact force of the CFRP-AM processes can be decomposed to the directions along/normal to the nozzle movement and the vertical build-up directions. The direction vectors are defined as $\mathbf{e}_t, \mathbf{e}_n$, and $\mathbf{e}_z$; the corresponding tangential, side, and vertical forces are defined as F_t, F_n, and F_z, respectively. In this work, the side force F_n and tangential force F_t provide a faster closed-loop (CL) control of the printing speed and the fiber extrusion, respectively. The vertical force is used to adjust the helical angle and the layer height slowly. These two major CL controls are illustrated in Fig. 5. The details of the controllers are discussed in Sections 3.1 and 3.2, respectively.

3.1. Velocity and fiber extrusion rate control with tangential and side force feedback

Consider the in-plane printing forces, the fiber tension, matrix material viscosity, and friction force contribute to a positive tangential force F_t; while the side force normal to the printing trajectory F_n is typically small in conventional printing conditions. The sudden increase typically arises from commonly seen fiber faults of lack of adhesion, as illustrated in Fig. 6. The faulty fiber will partly transmit the tension to the $\mathbf{e}_n$ direction and introduce irregular large F_n. In addition, the crystallization process of the semicrystalline thermoplastic matrix plays an essential role in the interlayer bond strength. Given that the crystallization state could not be directly observed in real-time in experiments, the side force is adopted as a valid observer to determine if the crystallization process at high curvature parts is sufficient to hold the fiber in place. Therefore, the magnitudes of F_n serve as a very typical abnormal signal and can be exploited to monitor and control the CFRP-AM process. Considering the matrix crystallization process at high printing speed is insufficient, interlayer bond strength can be enhanced and fiber misalignment can be alleviated by reducing printing speed. It has been shown in [24] that reducing the printing speed contributes to enhancing bond strength. The real-time contact force measurement provides a time-domain measurement of this potential fault, and a proxy fault signal u_n is constructed as

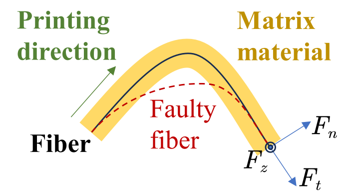

Fig. 6. Schematics of fiber directions and representative faults.

$$u_n = \begin{cases} |F_n| - F_{n,\max} & \text{when } |F_n| > F_{n,\max} \\ 0 & \text{when } |F_n| \leq F_{n,\max} \end{cases} \tag{22}$$

where $F_{n,\max}$ is the maximum allowable side force based on experiences and historical data. Note that $u_n \geqslant 0$ for all time. It is desirable to design a feedback mechanism that minimizes the printing speed when nonzero u_n is detected. The interference in the printing speed is also expected to stop once u_n returns to zero. This mechanism is conveniently realized by a first-order system given by

$$\delta\dot{V} = -\frac{\delta V}{T_n} + b_n u_n \tag{23}$$

where T_n is the time constant for the velocity regulation, b_n is the weight affecting the strength of the velocity reduction. With this definition, the actual printing velocity of the motion platform is dynamically adjusted to

$$V = \begin{cases} V_0 - \delta V & \text{when } V_0 - \delta V > V_{\min} \\ V_{\min} & \text{when } V_0 - \delta V \leqslant V_{\min} \end{cases} \tag{24}$$

where $V_{\min}$ is introduced to saturate the dynamic adjustment to make sure that the printing velocity is not too slow. This arises from the fact that the thermoplastic matrix material extrusion is typically slower than the printing velocity change and the fiber contact dynamics. Reducing the printing speed excessively may lead to undesirable over-extrusion of the matrix material. In this way, this fiber adhesion control detects an excessive amount of F_n and reduces the local speed correspondingly. The mechanism is highlighted in the yellow regions in Fig. 5.

Apart from the side force, the tangential force signal F_t serves as an effective feedback signal to mark the synchronization between the fiber extrusion and the motion of the printing platform. Insufficient fiber extrusion will lead to high tension forces, which further contributes to the high values of F_t. The fiber tension $F_{t,\max}$ is introduced as a warning threshold for excessive fiber tension. Similar to the proxy fault signal u_t

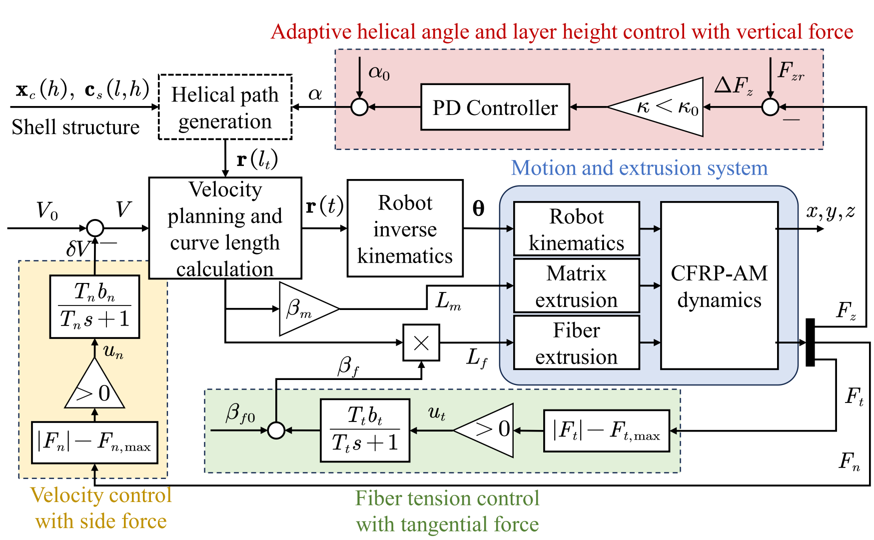

Fig. 5. Block diagram of the contact-force-based closed-loop feedback control of the CFRP-AM process.

for excessive fiber tension is defined as

$$u_t = \begin{cases} |F_t| - F_{t,\max} & \text{when} |F_t| > F_{t,\max} \\ 0 & \text{when} |F_t| \leq F_{t,\max} \end{cases} \tag{25}$$

Unlike the side force F_n that typically oscillates around zero, the tangential force is generally positive due to the fiber tension, viscosity, and friction. Maintaining the tangential force in desirable amplitudes also contributes to reducing the common adhesion fault shown in Fig. 6 at the corner and high curvature regions. Similarly, the fiber extrusion compensation signal is given by

$$\delta\dot{\beta}_f = -\frac{\delta\beta_f}{T_t} + b_t u_t \tag{26}$$

where T_t is the time constant for the velocity regulation, b_t is the coefficient for the fiber extrusion regulation, such that the fiber extrusion rate ratio is relaxed following

$$\beta_f = \begin{cases} \beta_{f,\max} & \text{when } \beta_{f0} + \delta\beta_f > \beta_{f,\max} \\ \beta_{f,\min} & \text{when } \beta_{f0} + \delta\beta_f > V_{\min} \\ \beta_{f0} + \delta\beta_f & \text{elsewhere} \end{cases} \tag{27}$$

The fiber extrusion rate is also saturated to ensure the fiber extrusion adjustment is within desirable range. The general fiber length should be very close to the trajectory length. With the dynamic adjustment of β_f, the fiber extrusion is given by

$$L_f = \int_0^t \beta_f V dt. \tag{28}$$

Note that both β_f and V are dynamically adjusted in this section. The fiber extrusion length is thus converted into the integration form. The mechanism for the fiber extrusion adjustment is highlighted in the green regions in Fig. 5.

3.2. Layer height and helical angle adaptation with vertical contact force feedback

The vertical force F_z can reflect the bonding condition between the newly deposited material and the previous layers. This work aims to dynamically adjust the printing layer height, exploiting this vertical force feedback. Unlike the CL control methods in Section 3.1 addressing the geometrical and local features, the printing height adjustment is expected to be slower for the height adjustment. The printing layer height adjustment is possible thanks to the helical printing trajectory generation framework proposed in Section 2.

To maintain a relatively stable contact force reference value F_{zr}, the vertical force error can be defined by

$$\Delta F_z = \begin{cases} F_{zr} - F_z & \text{when } \kappa \leq \kappa_0 \\ 0 & \text{when } L_m = \beta_m s, \kappa > \kappa_0 \end{cases} \tag{29}$$

where κ is the curvature in the current printing trajectory and κ_0 is its adjustment upper limit. The measurement indicates that the vertical force error signal is only recorded at low-curvature regions to adjust the helical angle. This choice arises from the CFRP-AM process characteristics exhibiting significant force patterns around the high-curvature regions. The irregular vertical force is due to the uneven surface at the high-curvature region caused by high fiber stiffness. Therefore, the layer height adjustment should avoid such regions.

The vertical force error signal is converted to the dynamic adjustment of the helical angle α through a proportional-derivative (PD) controller given by

$$\delta\alpha = K_p \Delta F_z + K_d \frac{d\Delta F_z}{dt} \tag{30}$$

where K_p and K_d are proportional and derivative coefficients, respectively. The helical angle is modified to

$$\alpha = \alpha_0 + \delta\alpha. \tag{31}$$

To avoid huge displacement of the motion platform, the saturation limitation is added to the $\delta\alpha$ such that $\delta_{\min} \leqslant \delta\alpha \leqslant \delta_{\max}$, where $\delta_{\min}$ and $\delta_{\max}$ are the lower and upper saturation limits, respectively. Note that in this CL control framework, the motion trajectory along the vertical direction and curve parameter direction is given by the integral framework during the helical regions of the trajectory, i.e.,

$$\frac{d}{dt}\hat{r}_z = V\sin\left(\frac{\alpha}{L_c(\hat{r}_z)}\right), \frac{d}{dt}\hat{l}_t = \frac{V}{L_c(\hat{r}_z)}\cos\left(\frac{\alpha}{L_c(\hat{r}_z)}\right) \tag{32}$$

The actual motion trajectory is achieved by

$$\hat{h} = \int (\alpha dl_t) dt \tag{33}$$

Note that in this framework, the layers to build the given shell structure are not certain since they depend on the dynamic adjustment of the printing trajectory. Therefore, an event trigger ($(h \geqslant H)$) is added to the dynamic control process to mark the completion of the printing. Activation of this trigger initializes the last layer of printing directly.

4. Experiment verification of proposed method

4.1. Experimental hardware setup

A robotic-based CFRP-AM system, shown in Fig. 7, is designed and built as the experimental platform for this study. An industrial 6-axis industrial robot (Huashu Co603), a continuous fiber and thermoplastic co-extrusion system (Anisoprint Composer A4), and a load cell (Hypersen HPS-FT060E) are integrated and controlled with Beckhoff TWINCAT real-time control system with EtherCAT communication and 1 kHz sampling rate. The co-extrusion system shown in Fig. 7(b) fuses the thermoplastic filament with the fiber prepreg in a heated chamber. The continuous fiber is also automatically cut in the co-extrusion system when a fiber path ends. The industrial robot moves to execute the printing trajectory by converting the printing trajectory to its joint space trajectory $\boldsymbol{\theta}$ via inverse kinematic calculations. During the printing process, the nozzle is fixed, and a glass plate is installed onto the end-effector of the industrial robot, with the load cell in the connection to measure the 3-axis contact force of the CFRP-AM process. The load cell used in this study is a rigid body with a light weight that has no impact

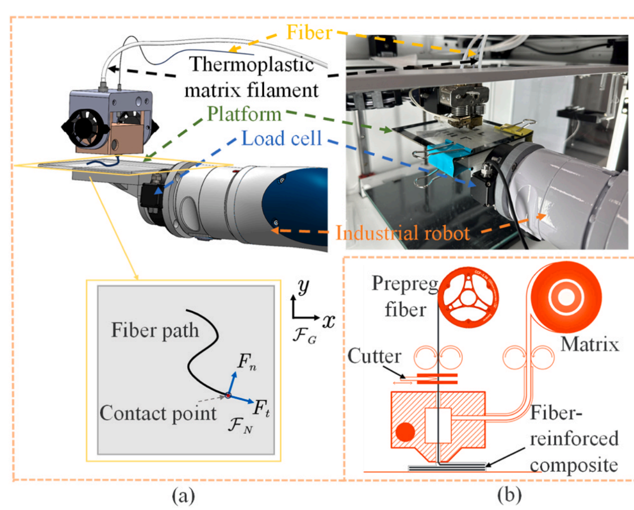

Fig. 7. Experimental setup. (a) Designed, fabricated, and assembled experimental platform with an industrial robot and load cell, and (b) schematics of co-extrusion system.

on the printing system. As shown in Fig. 7(a), the connector linking the contact point and the load cell is characterized by rigidity, ensuring that the forces measured by the load cell accurately correspond to the forces exerted at the contact point. This validation has been confirmed through a preliminary test. Define ground reference frame $\mathscr{F}_G$ and the nozzle fixed frame $\mathscr{F}_N$, all the vectors in $\mathscr{F}_G$ are labeled with superscript $^{(G)}$. The raw force signals obtained from the load cell are processed with zero calibration and median filtering, and are concatenated into a vector $\mathbf{f}^{(G)}$. The measurement is converted to the tangential, side, and vertical forces with the following relationship:

$$\{F_t \quad F_n \quad F_z\}^\top = [\mathbf{e}_t \quad \mathbf{e}_n \quad \mathbf{e}_z]^\top \mathbf{f}^{(G)} \tag{34}$$

where $\mathbf{e}_t$, $\mathbf{e}_n$ and $\mathbf{e}_z$ are directions defined in Section 3. The detailed CFRP-AM system parameters are listed in Table 1.

4.2. Experimental case studies

To verify the proposed contact force based CL CFRP-AM process control method established in Section 2, three closed shell structures were designed and printed to evaluate the control performances from different aspects.

- Case Study I: velocity and fiber extrusion CL control of a shallow rich-corner part,
- Case Study II: velocity and fiber extrusion CL control of a rich-curvature part and a rotated clover part, and
- Case Study III: helical angle and layer height CL control of a tapered cylinder.

These case studies aim to evaluate the fiber path deviations and the printing quality at various settings. To evaluate the turning angle's effect on the printing quality with and without CL control, shallow rich-corner parts with the same corner curvature are printed and evaluated in Case Study I, as shown in Fig. 8(a). To study the printing quality with different curvatures, rich curvature parts with variable curvature properties were printed and assessed in Case Study II, as shown in Fig. 8(b). Besides, rotated clover parts with higher complexity were printed and evaluated. To investigate the influence of fiber adhesion between layers on the printing quality, tapered cylinders with variable cross-sections were tested in Case Study III. Image analysis and 3D scanning are exploited to quantify the effectiveness of the CL control.

4.2.1. Case study I: velocity and fiber extrusion CL control of a shallow rich-corner part

To evaluate the performance with printing speed and fiber extrusion CL control, a shallow rich-corner with five layers was printed with the parameters in Table 2. The adoption of a shallow structure enables the camera to capture the top layer after printing, enabling the evaluation of printing errors with image analysis tools. In addition, the corners are designed to have 2-mm fillets to avoid printing sharp corners with stiff fiber prepreg. The rounded rich-corner shape is adopted as the reference printing path, and the composed points set $\{p_{r,1}, p_{r,2}, \ldots, p_{r,j}\}$ is defined as Ψ_r. The points set $\{p_{a,1}, p_{a,2}, \ldots, p_{a,j}\}$ that forms the actual printing path is defined as Ψ_a, obtained from the top layer images after image processing. To identify the deviation between the reference and actual path, contour error $e_{c,i}$ at point $p_{r,i}$ for each point is defined as

$$e_{c,i} = \min_{p_{a,j} \in \Psi_a} \left\{ \left\| p_{r,i}, p_{a,j} \right\| \right\} \tag{35}$$

where $\|.,.\|$ is the Euclidean distance between two points. Then, the Hausdorff distance e_h is applied and calculated by

$$e_h = \max\left\{ \max_{p_{r,i} \in \Psi_r} \{e_{c,i}\}, \max_{p_{a,j} \in \Psi_a} \{e_{c,i}\} \right\} \tag{36}$$

The fiber printing results shown in Fig. 9 illustrate the contour error of the printing process with and without FB control when the reference printing velocity V is 8 mm/s. Both configurations show that the printed curvature is smaller compared to the reference path. This is due to the significant fiber tension during sharp turns, resulting in inward deviations to mitigate large bending. Severe fiber misalignment is observed at corner regions on the top layer in Fig. 9(a). A closer view of the 90° corner in Fig. 9(a) reveals inner side fiber deviation on the inner lateral surface of the shell structure. Additionally, the fiber tracking error $e_{c,i}$ in Fig. 9(b) illustrates the obvious fiber deviations at corner regions and the maximum $e_{c,i}$ of the parts without FB control exceeds 2 mm.

By evaluating the enhancement quality of corners with different angles, the Hausdorff distance e_h at each corner is calculated and compared, separately, as shown in Fig. 9(c). The tracking error generally increases as the corner becomes sharper, indicating that it is challenging for the CFRP-AM process to turn sharp angles quickly due to fiber stiffness. When the corner angle is 150°, which is close to straight, the tracking error still exists but is small. The elastic force in the lightly bent fiber facilitates its recovery to the straight path and leads to misalignment. When printing with different reference velocities, the tracking error for all corner angles increases with velocity, as shown in Fig. 9(c). The higher velocity makes the deposited filament not fully solidified, while the bending-induced tensions easily leads to fiber misalignment. The obtuse-angle corners are more easily affected by the printing velocity.

With the application of FB control, the printed part at 8 mm/s exhibits improved geometry, with significantly reduced inner side fiber deviation observed in Fig. 9(a) and evident tracking error reduction as shown in Fig. 9(b). The maximum contour error for different corner angles with different reference velocities without and with FB control is plotted in Fig. 9(c). It can be seen that the maximum contour errors decrease significantly with FB control, which shows the effectiveness of the addition of FB control. The error reduction can reach around 50 % when the corner angles are 30° and 90°. When the corner angle reaches 120°, the quality enhancement with FB control is relatively limited. The controller maintains desirable performance when the reference velocity increases from 6 mm/s to 10 mm/s, though its efficiency becomes relatively attenuated when the velocity increases.

4.2.2. Case study II: printing speed and fiber extrusion FB control of a rich curvature part and a rotated clover part

To further assess the performance and robustness of printing speed and fiber extrusion CL control when dealing with varying curvatures, a 5-mm-height rich curvature part with increased complex geometry is introduced. The shape includes multiple arcs with different radii ranging from 1 mm to 8 mm, with details shown in Fig. 8(b) and printed with the parameters in Table 2. The fiber tension and the curvature of the fiber path lead to the inward deviation from the original fiber path. We purposely chose to use carbon fiber in black color and PLA matrix in white, such that the inner lateral surface of the printouts can serve as an effective evaluation tool for printing faults and misalignments. The black fiber regions are segmented and extracted by image processing; larger areas of black color indicate a higher percentage of fiber misalignments.

Table 1
Robotic-based CFRP-AM platform parameters.

Parameter	Values
Nozzle diameter	0.8 mm
Matrix material	Polylactic acid (PLA)
Continuous fiber	CCF−1.5 K
Nozzle temperature	210 °C
Printing size	120 mm × 120 mm
Fiber printing velocity	1–10 mm/s
Sampling time t_s	0.001 s

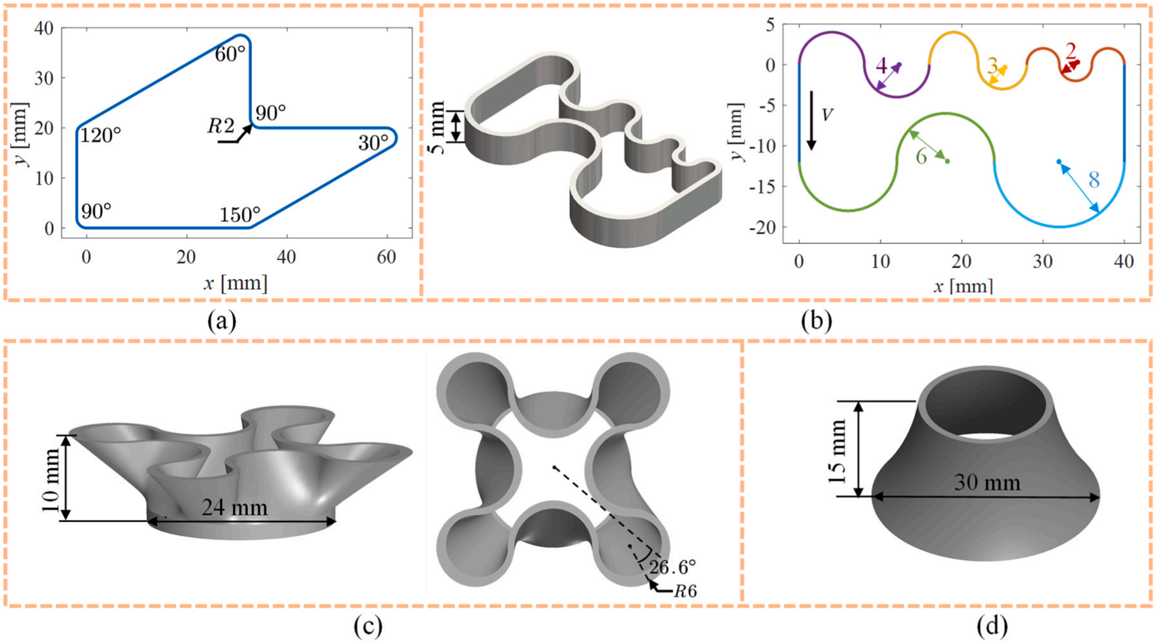

Fig. 8. 2D and 3D shapes of three case studies. (a) Case Study I: the shallow rich-corner part, (b)-(c) Case Study II: the rich-curvature part and the rotated clover part, (d) Case Study III: the tapered cylinder.

Table 2
Printing and control parameters for Case Studies I and II.

Parameters	Values
h_0 [mm]	0.2
$V, V_{\min}$ [mm/s]	[6,8,10], 3
β_m, β_{f0} [mm/mm]	0.2, 1
$F_{n,\max}, F_{t,\max}$ [N]	0.1, 0.5
T_n, T_t [s]	1, 2
b_n, b_t	20, 1
$\beta_{\max}, \beta_{\min}$ [mm/mm]	1.06, 0.95

The printed rich curvature parts are presented from different view angles in Fig. 10(a). The part without FB control exhibits evident fiber misalignment defects. In a certain layer in the middle, there is even a large segment of fibers completely detached from the printed part. This is destructive and indicates the undesirable robustness of the open-loop manufacturing process when printing complex shapes. Fiber misalignments happen in curved regions, particularly when the curvature is high. This alignment arises from the short solidification period, lack of sufficient bonding formation, and high fiber stiffness in the CFRP-AM process. Multiple views of printouts in Fig. 10(a) illustrate that deviated fibers appear at concave lateral surfaces, and the extracted fiber regions shown in Fig. 10(b) demonstrate poor printing quality without FB control. The printing quality further degrades with the increased curvature, as reported in Fig. 12. This arises from the high velocity, large traction force, and lack of layer adhesion. When applied with FB control, the printout shows an enhanced overall printing performance. When focusing on the defect-prone region, the fiber misalignment phenomenon is evidently reduced, which is observed from different view angles in Fig. 10(a) and obtained from extracted results in Fig. 10(b). As shown in Fig. 10, the misalignment fiber regions are significantly decreased

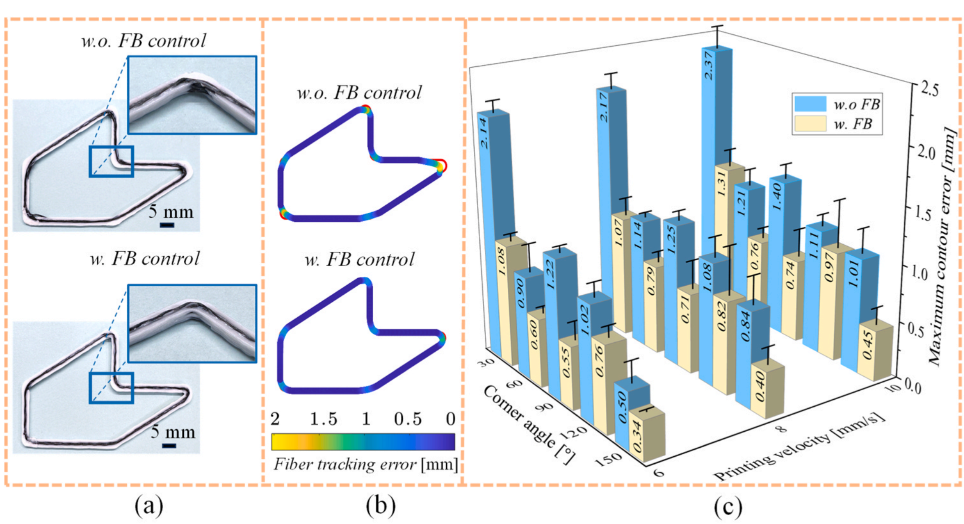

Fig. 9. Shallow rich-corner part printouts and analysis result without (w.o.) and with (w.) feedback (FB) control. (a) Printed parts with a zoomed view (velocity = 8 mm/s), (b) tracking error mapped to the printed rich-corner part (velocity = 8 mm/s), (c) Fiber printing path tracking error evaluation of different corner angles and printing velocities. The error bars represent ± SD from the mean value (n = 3).

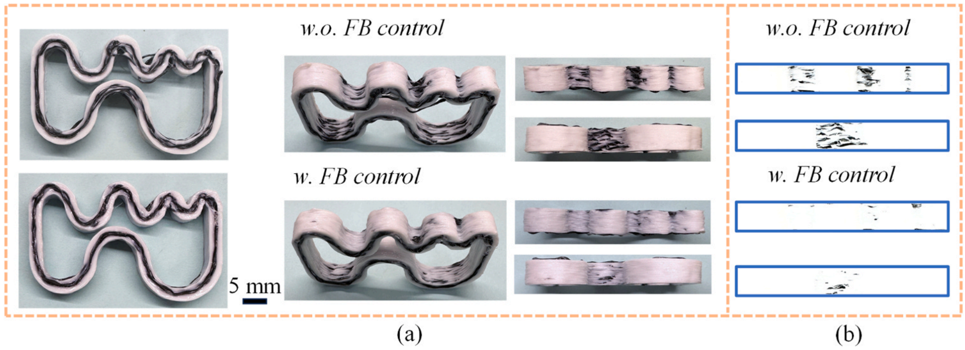

Fig. 10. Printed rich-curvature results without (w.o.) and with (w.) feedback (FB) control. (a) Parts with different view angles, and (b) extracted misaligned fiber region.

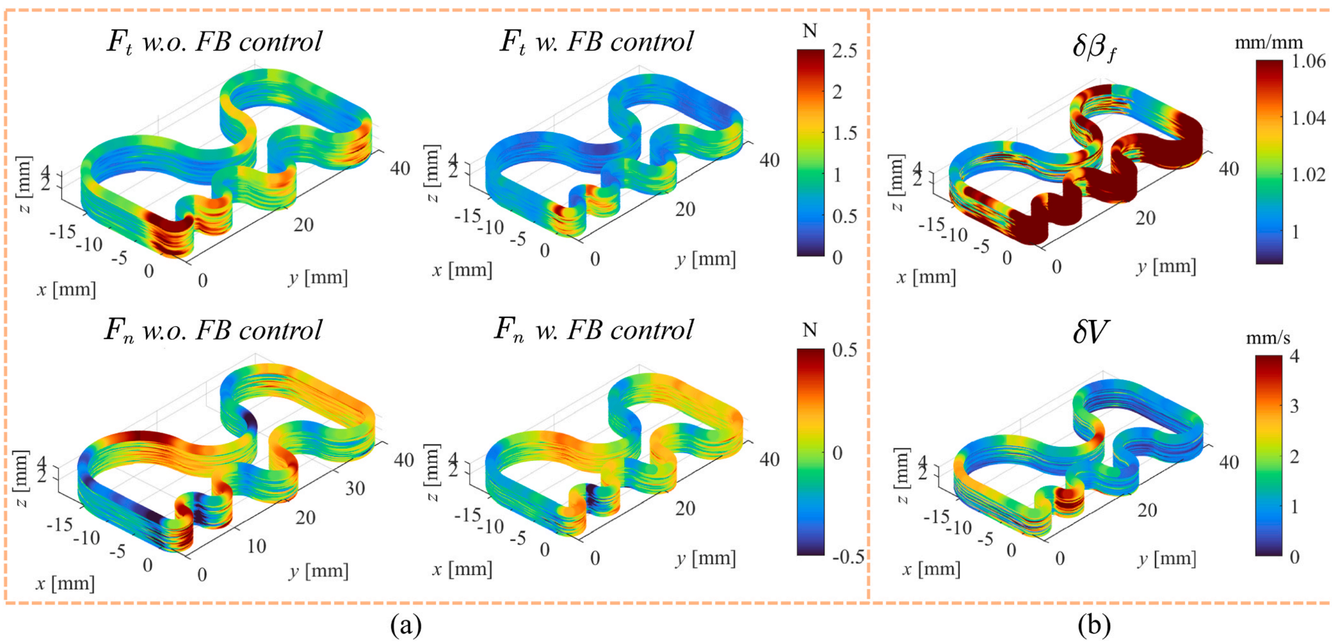

Fig. 11. Force trajectory and control signals mapped to the printed rich-curvature part without (w.o.) and with (w.) feedback (FB) control: (a) F_t (up) and F_n (down), (b) $\delta\beta_f$ (up) and δV (down).

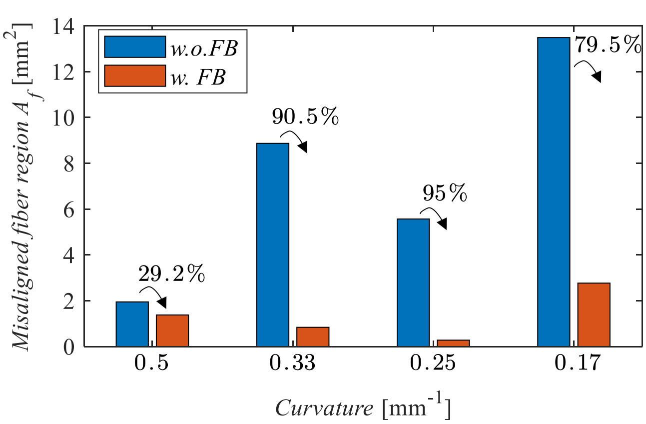

Fig. 12. Fiber misalignment region evaluation without (w.o.) and with (w.) feedback (FB) control.

with FB control, especially when the curvature is 0.33 mm^{-1} and 0.25 mm^{-1}. More than 90 % of the black region due to fiber deviations has been alleviated. For relatively large curvature 0.5 mm^{-1} regions, the enhancement of the FB controller drops to about 29.2 % since the printing process has already approached the maximum curvature that the machine can robustly fabricate. Overall, FB control significantly reduces fiber misalignment defects and performs different enhancements for different curvature features.

The contact force time history without and with control during the process is visualized in Fig. 11(a). In open-loop scenarios, the high values of contact forces often occur at curved regions, and values increase with curvature. The F_t and F_n can reach more than 2.5 N and 0.5 N respectively when the curvature is 0.5 mm^{-1}. The abnormal contact forces are consistent with the fiber misalignment in printed parts shown in Fig. 10. Accordingly, as the contact force map shows in Fig. 11 (a), the large values of F_t at the large curvature regions are reduced when the feedback control is introduced. The side force F_n also exhibits a reduction compared to open-loop control, particularly at high values. Fig. 11(b) shows the generated compensation signals during printing. The large δV often occurs at large curvature regions and their neighborhoods, and β_f increases when the printing trajectory has large curvatures, which aligns with the intuition for parameter tuning. These results illustrate the effectiveness of the proposed methods in addressing the local geometrical features of the CFRP-AM process.

To verify the efficiency of the FB controller when applied to complex structures, a rotated clover part with non-uniform cross-sections shown in Fig. 8(c) is printed with the parameters in Table 2. Similarly to the rich-curvature part, the black fiber regions at concave surfaces of the rotated clover part indicate fiber misalignments and are segmented and extracted by image processing. The higher black area ratio R_{fm} indicates a higher fiber misalignment probability, which is defined by

$$R_{fm} = \frac{A_f}{A_p} \tag{37}$$

where A_f is the misaligned fiber area and A_p is the area of the printed part projected in a representative view angle (Fig. 13(a)). The view angle is selected to observe the fiber misalignment in different directions for image analysis tools. Fiber inward deviations are severe without FB control at concave surfaces and are represented by huge black regions, as shown in Fig. 13(b). The estimated R_{fm} in the open-loop scenario is 5.92 %. With the FB controller, the misaligned black fibers (marked by R_{fm}) at lateral surfaces are significantly decreased to 0.47 %. This 92.06 % R_{fm} reduction with FB control demonstrates the effectiveness of the FB controller when handling complex structures.

4.2.3. Case study III: helical angle and layer height control of a tapered cylinder

To identify the influence of layer height h_0 on the vertical contact force F_z, a series of open-loop printing experiments were performed, and the results are summarized in Fig. 14. The valid testing layer height varies from 0.15 mm (where fiber abrasion occurs) to 0.7 mm (where bonding failure occurs). An 8-layer cylinder with helical trajectory is printed, and the average vertical force in the middle 6 layers is measured for data fitting. The fitted vertical contact force formulates a nonlinear function as shown in Fig. 14. The fitted function is expressed as $F_z = Ah_0^B$, with parameters $A = 0.059$ N/mm and $B = -1.576$. Exponential decay of the contact force regarding the layer height is observed. To avoid fiber abrasion and interlayer detachment, the contact forces in the middle range (e.g., 0.3 N to 0.9 N) are selected as reference forces for feedback control.

Unlike previous cases with a uniform cross-section, this section exploits a tapered cylinder, as shown in Fig. 8(c), to evaluate the performance with layer height CL control. The changing cross-sections place higher demands on the connections between the layers and radius R_t ia a function of height h expressed by $R_t(h) = R_0 C^{-h/D}$, where $R_0 = 15$mm, $C = 3$, and $D = 30$ mm. The parts were printed with parameters in Table 3 and shown in Fig. 16(a). An EinScan Pro HD optical 3D scanner measures the accuracy of the external surface geometry of printed parts under different control conditions. The printed part is scanned in full view and assisted by the rotation stage. With the obtained 3D points (x_m, y_m, z_m), the measured radius R_m for each point on the revolving model is obtained by

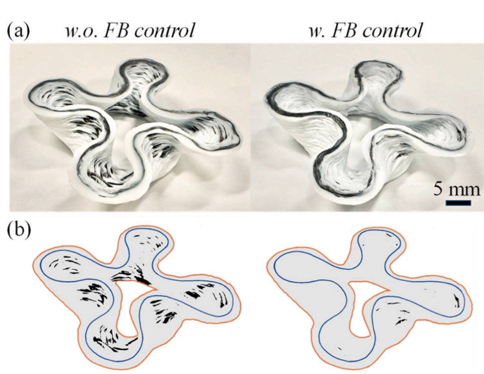

Fig. 13. Printed results of a rotated clover structure without (w.o.) and with (w.) feedback (FB) control. (a) Printed parts and (b) extracted misaligned fiber region.

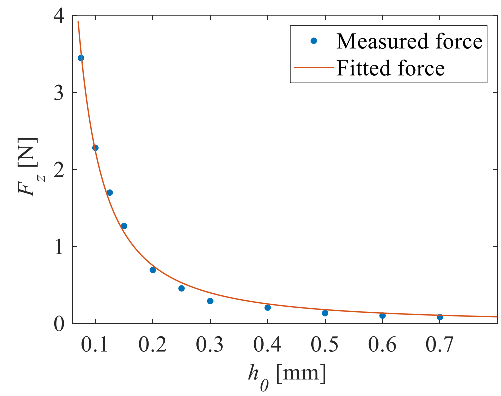

Fig. 14. Relationship between layer height and contact force.

$$R_m = \sqrt{x_m{}^2 + y_m{}^2} \tag{38}$$

The desired radius R_d for each point is calculated given the measured height z_m. The radius error e_r for each measured point is thus obtained by

$$e_r = R_d - R_m \tag{39}$$

The vertical contact force shown in Fig. 15(a) illustrates that the first layer typically has a higher contact force to guarantee a solid connection between the deposited fiber and platform, while the contact force drops significantly without the FB control, indicating a relatively weak layer adhesion. Note that the vertical contact force quickly drops to around 0.1 N without FB control. In contrast, with the feedback introduced from the second layer, the vertical contact force is maintained at around the corresponding reference force during the entire printing process, indicating an enhanced level of layer adhesion. When the reference forces increase, the actual vertical forces produce larger fluctuations, because the forces become more sensitive to layer height as shown in Fig. 14. Slight height adjustment results in huge force variation, which limits the control ability of this closed-loop system. Additionally, the larger vertical forces are accompanied by larger tangential forces and side forces. This is due to the increase in normal pressure among the fiber, nozzle, and platform, which leads to an increase of the perpendicular friction, resulting in the increase of F_t and F_n. As mentioned in Section 4.2.2, the huge F_t and F_n will increase the risk of fiber deviation from the desired trajectory when passing large curvature regions, leading to fiber misalignment issues.

The printouts without and with FB control are shown in Fig. 16(a). It is obvious that when the vertical force increases, the outer surfaces of the printed parts produce higher accuracy. Particularly, the connections between layers are weak for the part printed without FB control. The surface geometry errors of the printed parts are reduced as the vertical force reference increases, as shown in the constructed surface error map in Fig. 16(b). The root mean square error (RMSE), maximum error, and error range of each part are measured and listed in Table 4, indicating an error reduction of up to 66.3 %. The highest surface quality with the lowest RMSE is achieved when the contact force reference is 0.6 N, which indicates a desirable reference contact force. When the contact force reference is further increased to 0.9 N, the printing quality is generally preserved, but the increase in contact force leads to enhanced interlayer adhesion, decreased layer height, and more fiber usage. In addition, high vertical force reference tends to increase the fluctuation of the other contact forces F_t and F_n (as Fig. 15 shows).

5. Conclusions

This study proposes a novel approach to enhance the quality of the material extrusion CFRP-AM process. The proposed helical CFRP-AM

Table 3
Printing and control parameters for Case Study III.

Parameters	h_0	V	β_m	β_f	K_p	K_d	δ_{min}	δ_{max}
Values	0.5 mm	3 mm/s	0.3 mm/mm	1 mm/mm	0.36 mm	1 mm	−0.3 mm	0.3 mm

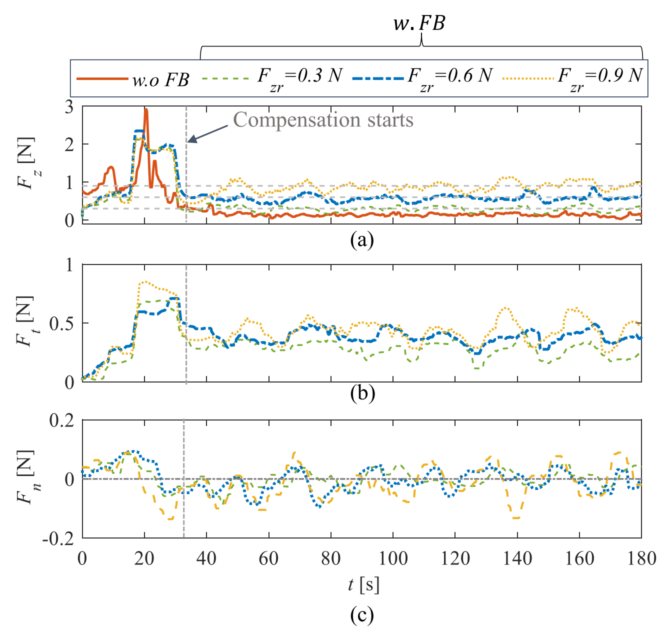

Fig. 15. Force signal time history during printing without (w.o.) and with (w.) feedback (FB) control. (a) F_z, (b) F_t, and (c) F_n.

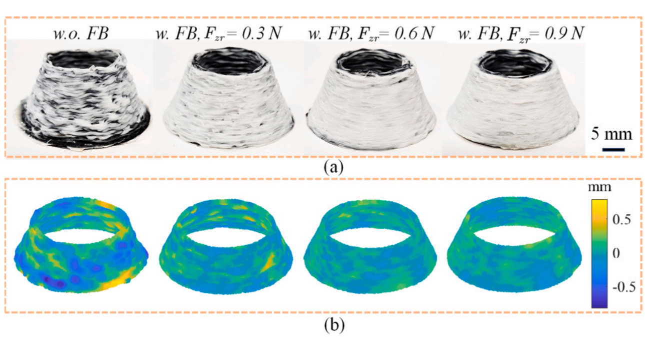

Fig. 16. Printed results of tapered cylinder without (w.o.) and with (w.) feedback (FB) control. (a) Printed parts, and (b) surface error map.

Table 4
Multi-dimensional surface error evaluation with and without FB control.

Test	F_{zr} (N)	RMSE (mm)	Max error (mm)	Error reduction (%)	Fiber usage (mm)	Average layer height (mm)
w.o. FB	-	0.211	0.829	-	2364.894	0.5
w. FB	0.3	0.116	0.484	45.02	3957.353	0.283
	0.6	0.079	0.320	62.56	4931.490	0.231
	0.9	0.087	0.280	58.77	5705.429	0.196

printing trajectory generation method for closed shell structures creates a continuous feedback control environment for dynamic adjustment without fiber cutting. By exploiting contact forces as the major feedback control signals, an integrated closed-loop printing system is developed, enabling dynamic and rapid adjustment of the feed velocity, layer height, and fiber extrusion rate. The following conclusions can be drawn:

- A fundamental understanding of the relationship among the contact forces, printing parameters, and product quality has been presented. The contact forces in the CFRP-AM process are divided into tangential force, side force, and vertical force according to their direction. The increased tangential force indicates an increase in fiber tension, particularly in printing large curvature regions, which leads to fiber misalignment. The tangential force based controller by increasing fiber extrusion effectively alleviates fiber tension, illustrated by improved fiber tracking accuracy and decreased abnormal tangential forces. The side force has been proven an effective observer of the crystallization process, and its related controller by decreasing printing velocity reduces fiber misalignment, by providing sufficient solidification time to facilitate fiber-matrix bonding. Additionally, vertical force is related to the layer height and directly influences interlayer bonding. Decreasing layer height with increased vertical force has been proven to enhance surface quality. Combining these closed-loop controllers reduces the layer adhesion fault, thus enhancing the printing quality locally, particularly in addressing the drop in printing quality at high-curvature regions of the parts.
- An in-depth verification of the controller in fabricating multi-complexity parts under different printing conditions has been completed. The proposed closed-loop control methods were verified in a robotic co-extrusion CFRP-AM system with a load cell measuring the dynamic contact force. The case studies including a shallow rich-corner part with different turning angles, a rich-curvature part with multiple curvatures, a rotated clove part with high geometric complexity, and a tapered cylinder with varied cross-sections were printed and evaluated. Printing quality enhancements were observed in all case studies, demonstrated by reduced fiber tracking error on a single layer, reduced fiber misaligned area on the lateral surface, and overall improved surface quality. The parts containing different geometric features were also printed at different velocities and all showed quality enhancement with the application of feedback control, which verifies the uniformity and efficiency of the controller in enhancing printing quality at different conditions.

In conclusion, this research first exploits contact force in a CFRP-AM process as a signal for real-time closed-loop control, which has the advantage of handling uncertainties and complexities during the high-dynamic manufacturing process. This proposed method shows significant potential for printing complex CFRP parts (such as aerostructures) of high quality that can be used in wide applications.

CRediT authorship contribution statement

Yuexin YANG: Writing – review & editing, Writing – original draft, Visualization, Validation, Software, Methodology, Investigation, Formal analysis, Data curation. **Molong Duan:** Writing – review & editing, Supervision, Resources, Project administration, Methodology, Funding acquisition, Conceptualization. **Yi ZHOU:** Software, Investigation, Data curation.

Declaration of Generative AI and AI-assisted technologies in the writing process

The writing process only uses ChatGPT and Grammarly AI to perform grammar checks.

Declaration of Competing Interest

The authors declare that they have no known competing financial interests or personal relationships that could have appeared to influence the work reported in this paper.

Acknowledgments

The authors acknowledge support from the Research Grants Council (RGC) of the Government of Hong Kong Special Administrative Region (HKSAR) with RGC/ECS Project (No. 26215824), HKUST research equipment development fund, and HKUST Bridge Gap Fund (BGF). This work was supported in part by the Project of Hetao Shenzhen-Hong Kong Science and Technology Innovation Cooperation Zone (HZQB-KCZYB-2020083). Profs. Kai Tang, Tianlong Zhang, and Hongyu Yu provided valuable feedback on this work. Dr. Mark Ellwood provided proofreading and English editing. The help from the funding agency and the other researchers is sincerely appreciated.

References

[1] Goh, G.D., Toh, W., Yap, Y.L., Ng, T.Y., Yeong, W.Y., 2021. Additively manufactured continuous carbon fiber-reinforced thermoplastic for topology optimized unmanned aerial vehicle structures. Compos B Eng. 216, 108840 https://doi.org/10.1016/j.compositesb.2021.108840.

[2] Wang, X., Jiang, M., Zhou, Z., Gou, J., Hui, D., 2016. 3D printing of polymer matrix composites: a review and prospective. Compos B Eng. 110 https://doi.org/10.1016/j.compositesb.2016.11.034.

[3] Penumakala, P.K., Santo, J., Thomas, A., 2020. A critical review on the fused deposition modeling of thermoplastic polymer composites. Compos B Eng. 201, 108336 https://doi.org/10.1016/j.compositesb.2020.108336.

[4] He, S., Ma, P.-C., Duan, M., 2024. Continuous fiber path optimization in additive manufacturing: a gradient-based b-spline finite element approach. Addit. Manuf. 86, 104155. https://doi.org/10.1016/j.addma.2024.104155.

[5] Li, N., Li, Y., Liu, S., 2016. Rapid prototyping of continuous carbon fiber reinforced polylactic acid composites by 3D printing. J. Mater. Process Technol. 238, 218–225. https://doi.org/10.1016/j.jmatprotec.2016.07.025.

[6] Chen, R., Bratten, A., Rittenhouse, J., Leu, M.C., Wen, H., 2023. Additive manufacturing of continuous carbon fiber-reinforced SiC ceramic composite with multiple fiber bundles by an extrusion-based technique. Ceram. Int 49, 9839–9847. https://doi.org/10.1016/j.ceramint.2022.11.157.

[7] Zhuo, P., Li, S., Ashcroft, I.A., Jones, A.I., 2021. Material extrusion additive manufacturing of continuous fibre reinforced polymer matrix composites: A review and outlook. Compos B Eng 224, 109143. https://doi.org/10.1016/j.compositesb.2021.109143.

[8] Wang, F., Wang, G., Ning, F., Zhang, Z., 2021. Fiber–matrix impregnation behavior during additive manufacturing of continuous carbon fiber reinforced polylactic acid composites. Addit. Manuf. 37, 101661 https://doi.org/10.1016/j.addma.2020.101661.

[9] Akhoundi, B., Behravesh, A.H., Bagheri Saed, A., 2019. Improving mechanical properties of continuous fiber-reinforced thermoplastic composites produced by FDM 3D printer. J. Reinf. Plast. Compos. 38, 99–116. https://doi.org/10.1177/0731684418807300.

[10] Lu, L., Hou, J., Yuan, S., Yao, X., Li, Y., Zhu, J., 2023. Robotics and computer-integrated manufacturing deep learning-assisted real-time defect detection and closed-loop adjustment for additive manufacturing of continuous fiber-reinforced polymer composites. Robot Comput. Integr. Manuf. 79, 102431 https://doi.org/10.1016/j.rcim.2022.102431.

[11] Khosroupour Arabi, M., Kordani, N., 2023. 3D-printing of continuous fiber: a review of processes, materials and properties. Polym. Plast. Technol. Mater. https://doi.org/10.1080/25740881.2023.2222793.

[12] Li, N., Link, G., Jelonnek, J., 2020. 3D microwave printing temperature control of continuous carbon fiber reinforced composites. Compos Sci. Technol. 187, 107939 https://doi.org/10.1016/j.compscitech.2019.107939.

[13] Yao, J., Duongthipthewa, A., Xu, X., Liu, M., Xiong, Y., Zhou, L., 2024. Interlayer bonding improvement of PEEK and CF-PEEK composites with laser-assisted fused deposition modeling. Compos. Commun. 45, 101819 https://doi.org/10.1016/j.coco.2024.101819.

[14] Liu, T., Tian, X., Zhang, Y., Cao, Y., Li, D., 2020. High-pressure interfacial impregnation by micro-screw in-situ extrusion for 3D printed continuous carbon fiber reinforced nylon composites. Compos Part A Appl. Sci. Manuf. 130, 105770 https://doi.org/10.1016/j.compositesa.2020.105770.

[15] Chen, S., Yang, Y., Liu, S., Duan, M., 2023. In-situ additive manufacturing deposition trajectory monitoring and compensation with thermal camera. Addit. Manuf. 78, 103820 https://doi.org/10.1016/j.addma.2023.103820.

[16] Mercado, F., Rojas Arciniegas, A., 2020. Additive manufacturing methods: techniques, materials, and closed-loop control applications. Int. J. Adv. Manuf. Technol. 109 https://doi.org/10.1007/s00170-020-05663-6.

[17] Lu, L., Hou, J., Yuan, S., Yao, X., Li, Y., Zhu, J., 2023. Deep learning-assisted real-time defect detection and closed-loop adjustment for additive manufacturing of continuous fiber-reinforced polymer composites. Robot Comput. Integr. Manuf. 79, 102431 https://doi.org/10.1016/j.rcim.2022.102431.

[18] De Backer, W., Sinkez, P., Chhabra, I., Van Tooren, M.J., Bergs, A., 2020. In-Process Monitoring of Continuous Fiber Additive Manufacturing through Force/Torque Sensing on the Nozzle. In: AIAA Scitech 2020 Forum. American Institute of Aeronautics and Astronautics, Reston, Virginia. https://doi.org/10.2514/6.2020-1632.

[19] Il Lee, W., Springer, G.S., 1987. A model of the manufacturing process of thermoplastic matrix composites. J. Compos Mater. 21, 1017–1055. https://doi.org/10.1177/002199838702101103.

[20] Zhang, J., Zhou, Z., Zhang, F., Tan, Y., Yiwen, T., Yang, B., 2020. Performance of 3D-printed continuous-carbon-fiber-reinforced plastics with pressure. Materials 13, 471. https://doi.org/10.3390/ma13020471.

[21] Cheng, P., Wang, K., Chen, X., Wang, J., Peng, Y., Ahzi, S., Chen, C., 2021. Interfacial and mechanical properties of continuous ramie fiber reinforced biocomposites fabricated by in-situ impregnated 3D printing. Ind. Crops Prod. 170, 113760 https://doi.org/10.1016/j.indcrop.2021.113760.

[22] Zhang, Z., Long, Y., Yang, Z., Fu, K., Li, Y., 2022. An investigation into printing pressure of 3D printed continuous carbon fiber reinforced composites. Compos Part A Appl. Sci. Manuf. 162, 107162 https://doi.org/10.1016/j.compositesa.2022.107162.

[23] Bettini, P., Alitta, G., Sala, G., Di Landro, L., 2017. Fused deposition technique for continuous fiber reinforced thermoplastic. J. Mater. Eng. Perform. 26, 843–848. https://doi.org/10.1007/s11665-016-2459-8.

[24] Tian, X., Liu, T., Yang, C., Wang, Q., Li, D., 2016. Interface and performance of 3D printed continuous carbon fiber reinforced PLA composites. Compos Part A Appl. Sci. Manuf. 88, 198–205. https://doi.org/10.1016/j.compositesa.2016.05.032.